

Evidence of Ultrashort Orbital Transport in Heavy Metals Revealed by Terahertz Emission Spectroscopy

Tongyang Guan^{1,2,§}, Jiahao Liu^{1,2,§}, Wentao Qin^{1,2}, Yongwei Cui^{1,2}, Shunjia Wang^{1,2},
Yizheng Wu^{1,2,*}, Zhensheng Tao^{1,2,*}

¹State Key Laboratory of Surface Physics and Key Laboratory of Micro and Nano Photonic Structures (MOE), Department of Physics, Fudan University, Shanghai 200433, P R China.

²Shanghai Key Laboratory of Metasurfaces for Light Manipulation, Fudan University, Shanghai 200433, P R China.

§ These authors contributed equally to this work.

* Corresponding authors: wuyizheng@fudan.edu.cn; zhenshengtao@fudan.edu.cn.

Abstract

The orbital angular momentum of electrons offers a promising, yet largely unexplored, degree of freedom for ultrafast, energy-efficient information processing. As the foundation of orbitronics, understanding how orbital currents propagate and convert into charge currents is essential – but remains elusive due to the challenge in disentangling orbital and spin dynamics in ultrathin films. Although orbital currents have been predicted to propagate over long distances in materials, recent theoretical studies argue that lattice symmetry may constrain their mean free paths (MFPs) to the scale of a single atomic layer. In this work, we provide the first direct experimental evidence for ultrashort orbital MFPs in heavy metals (HMs) – W, Ta, Pt – revealed by femtosecond terahertz emission spectroscopy. This is enabled by sub-nanometer-precision control of thin-film thickness using wedge-shaped HM|Ni heterostructures. By employing a multi-component terahertz-emission model, we quantitatively extract the orbital MFPs, consistently finding them shorter than their spin counterparts. Furthermore, control experiments *rule out* interfacial orbital-to-charge conversion as the dominant mechanism, confirming that the process is governed by the bulk inverse orbital Hall effect. Our findings resolve a central controversy in orbitronics and provide key insights into orbital transport and conversion mechanisms.

Orbitronics is an emerging field that explores the control and manipulation of electronic orbital angular momentum (L) in solid-state systems, opening new pathways for information processing and storage¹⁻⁴. Compared to spin angular momentum (S), which underpins conventional spintronics⁵⁻⁷, the ability to manipulate L provides several key advantages. First, due to the larger angular momentum that orbital degrees of freedom can carry, L -induced torques have been theoretically predicted⁸⁻¹⁰ and experimentally demonstrated¹¹⁻¹⁵ to enable highly efficient manipulation of magnetic order. Second, orbital currents, which are the flows of L , have been reported to propagate over long distances, enabling the excitation of magnetic moments far from material interfaces. Both experimental^{11,15-17} and theoretical¹⁸ studies have indicated such long-range orbital transport in various materials. In particular, recent femtosecond laser-excited terahertz emission spectroscopy in magnetic heterostructures has revealed orbital mean free paths (MFPs) up to 80 nm in non-magnetic metals¹⁹⁻²¹. Furthermore, these studies have suggested an interfacial orbital-to-charge conversion mechanism via the inverse orbital Rashba-Edelstein effect (IOREE)¹⁹⁻²¹.

Although the potential of orbitronics is compelling, substantial experimental challenges and fundamental scientific questions remain unresolved. A major experimental difficulty lies in distinguishing between spin and orbital contributions. Currently, none of the electrical^{12,16,17,22} or optical^{11,15,19-21} techniques can unambiguously separate spin and orbital signals, and spin-orbit coupling (SOC) within materials enables mutual conversion between them. Although X-ray²³ and electron²⁴ magnetic circular dichroism has the potential to discriminate between S and L , direct

observation of orbital transport remains challenging. In many prior studies, contributions from spin currents, often from Ni, were overlooked in the data interpretation, sometimes with low SOC materials being employed. For the same reason, it is uncertain whether the observed orbital signals arise from intrinsic bulk conversions or from interfacial conversion effects.

From a theoretical perspective, first-principles calculations have indicated that the propagation of orbital currents may still be confined to distances shorter than a single atomic layer, due to the stringent constraints imposed by crystal lattice symmetry^{25–27}. Given such potentially ultrashort orbital MFPs, experimental access to ultrathin film regimes with sub-nanometer precision is essential for resolving this prediction. However, this critical parameter space remains largely underexplored.

In this work, we present the first experimental evidence of ultrashort orbital MFPs in heavy metals (HMs), revealed by terahertz emission spectroscopy on nanometer-scale HM|ferromagnet (FM) heterostructures. This is enabled by sub-nanometer-precision control of HM-layer thicknesses in the ultrathin (<5 nm) regime. In particular, in W|Ni heterostructures, we observe nearly complete cancellation of the terahertz radiation at a critical W-layer thickness of ~3.0 nm, where the orbital- and spin-induced signals are nearly equal in magnitude but opposite in polarity. This phenomenon provides direct evidence that the orbital MFP (λ_L) is shorter than the spin MFP (λ_S) in W. By fitting the experimental results to a multi-component terahertz-emission model, we quantitatively extract λ_L for different HMs (W, Ta and Pt), consistently finding that λ_L is shorter than λ_S . The extracted amplitudes and polarities of the spin and orbital

signals are consistent with first-principles calculations^{9,28,29}. Furthermore, our analysis *rules out* interfacial orbital-to-charge and spin-to-charge conversion as dominant mechanisms, supporting that the observed signals arise from intrinsic bulk processes via the inverse orbital Hall effect (IOHE) and inverse spin Hall effect (ISHE).

Experimental Principle

Figure 1 illustrates the fundamental principle of our experiment. When a femtosecond laser pulse excites HM|FM heterostructures, ultrafast spin (j_S) and orbital (j_L) currents are simultaneously generated in the FM layer. The polarizations of S and L in the FM layer are aligned by an external magnetic field H . Both currents propagate along the z axis from the FM layer into the HM layer, where spin-to-charge and orbital-to-charge conversions generate in-plane charge currents that emit terahertz radiation.

In this study, Ni and Fe are selected as FM metals due to their high efficiency in generating orbital and spin currents, respectively^{30,31}. Various HMs, including W, Ta and Pt are chosen based on their distinct polarities for spin (γ_{SH}) and orbital (γ_{OH}) Hall angles^{9,29,32}, as well as their different λ_L and λ_S values. All heterostructures are grown on Al₂O₃(0001) substrates, pre-coated with a 4-nm SiO₂ buffer layer. The samples are capped with a 4-nm SiO₂ protective layer to prevent oxidation.

Through this manuscript, the notation “HM|FM” refers to the growth sequence of the heterostructure on the substrate and the SiO₂ buffer layer. For clarity, the SiO₂ buffer and capping layers are omitted from the labeling unless otherwise specified.

To distinguish spin and orbital contributions and systematically investigate their propagation in HMs, we fabricate wedge-shaped samples where the HM-layer

thickness (d_{HM} , HM=W, Ta, Pt) varies continuously along the x -axis. The FM-layer thickness (d_{FM} , FM=Ni, Fe) is fixed at 5 nm. By scanning the sample along x with respect to the laser spot, we obtain terahertz signals as a function of d_{HM} using free-space terahertz electro-optical sampling^{33,34}. The wedge-shaped design provides two key advantages: (i) it enables terahertz emission measurements across a continuous range of d_{HM} with sub-nanometer resolution, and (ii) it mitigates ambiguities associated with growth-condition variations in different samples. Further details about sample preparation, characterization, and experimental setups are provided in the Methods and Supplementary Materials (SM) Section S1.

Terahertz Signals from Different Heterostructures

In Fig. 2, we present the terahertz signals obtained from HM|Ni and HM|Fe, where the HM materials are W (Figs. 2a-c), Ta (Figs. 2d-f) and Pt (Figs. 2h-j). The terahertz waveforms as a function of d_{HM} are shown in Figs. 2b-j, while the terahertz peak amplitudes extracted at time $t=0$ are plotted in Figs. 2a, d, and h.

Distinct terahertz emission behaviors are observed depending on the FM-layer composition. In the Fe-based heterostructures (W|Fe in Fig. 2c, Ta|Fe in Fig. 2f, and Pt|Fe in Fig. 2j), the terahertz signal polarities are consistent with the spin Hall angles (γ_{SH}) of the respective HMs, indicating that terahertz generation is predominantly driven by spin currents and ISHE³⁵⁻³⁷.

In stark contrast, the HM|Ni heterostructures exhibit notably different behaviors. In W|Ni (Figs. 2a-b), the terahertz signal reverses its polarity at $d_{\text{W}} \approx 3.0$ nm, with its amplitude peaking at $d_{\text{W}} \approx 0.8$ nm. In the case of Ta|Ni (Figs. 2d-e), the terahertz polarity

is opposite to that of Ta|Fe but aligns with Pt|Fe (Fig. 2j), despite the opposite γ_{SH} signs of Ta and Pt^{9,21,29}. Furthermore, the terahertz peak amplitude of Ta|Ni exhibits a sharper rise with increasing d_{Ta} , compared to Ta|Fe (Fig. 2d). In Pt|Ni (Fig. 2i), although the terahertz signal shares the same polarity as Pt|Fe, the amplitude rises slightly faster with increasing d_{Pt} . These results cannot be fully explained by ISHE alone, strongly suggesting an important contribution from orbital-to-charge conversion^{19,21}.

Disentangling Terahertz Contributions from Spin and Orbital Currents

The polarity reversal in the terahertz signal of W|Ni (Figs. 2a-b) strongly suggests the coexistence of competing terahertz generation mechanisms characterized by distinct MFPs in W. This behavior can be explained by the theoretical predictions that W possesses opposite spin Hall (γ_{SH}) and orbital Hall (γ_{OH}) angles, where $\gamma_{\text{SH}} < 0$ and $\gamma_{\text{OH}} > 0$ ^{9,29,32}. Notably, at large d_{W} (> 3 nm), the negative terahertz polarity of W|Ni aligns with that of W|Fe (Fig. 2a), indicating that ISHE-driven spin-to-charge conversion dominates. In contrast, at ultrathin W layers ($d_{\text{W}} < 3$ nm), the positive polarity suggests that orbital-to-charge conversion becomes the dominant source, contributing via the IOHE. The crossover at $d_{\text{W}} \approx 3.0$ nm thus indicates that the orbital MFP (λ_L) is shorter than the spin MFP (λ_S) in W.

For Ta|Ni and Pt|Ni, although no polarity reversal is observed, the terahertz amplitudes in both cases peak at shorter HM thicknesses, compared to their Fe-based counterparts (Figs. 2d and h). These results also imply shorter λ_L than λ_S in Ta and Pt.

Beyond the above qualitative analysis, a quantitative understanding requires modeling all contributing sources of terahertz emission in HM|Ni heterostructures. In

addition to the spin and orbital signals, the anomalous Hall effect (AHE)^{21,38,39} and magnetic dipole emission (MDE)⁴⁰⁻⁴² in the ferromagnetic Ni layer may contribute to the terahertz signals. To assess the role of the Ni layer, we experimentally measured terahertz emission from a 5-nm Ni film encapsulated between the substrate and the capping layer. These measurements reveal that the Ni layer generate comparable terahertz signals via the AHE and MDE. Notably, the Ni-layer signal is non-negligible when compared to the total terahertz emission from HM|Ni samples (see SM Section S2).

Based on these findings, we construct a multi-component terahertz-emission model (MC-TEM), in which the total terahertz emission from HM|Ni is described as a superposition of three components:

$$E(t, d_{\text{HM}}) = A_S(d_{\text{HM}})\mathcal{E}_S(t) + A_L(d_{\text{HM}})\mathcal{E}_L(t) + A_{\text{Ni}}(d_{\text{HM}})\mathcal{E}_{\text{Ni}}(t), \quad (1)$$

where the first two terms represent the spin and orbital signals, and the third term accounts for the terahertz radiation solely from the Ni layer. In Eq. (1), the amplitude terms A_m ($m=S, L, \text{Ni}$) depend on the HM thickness d_{HM} , while $\mathcal{E}_m(t)$ captures the temporal waveform of each contribution. This decomposition is supported by the generally shiftless terahertz waveforms shown in Figs. 2b-j (see Methods).

Considering the effects of optical absorption, interfacial reflections of spin and orbital currents, and the shunting effect from adjacent layers, we obtain³⁷:

$$A_{S(L)}(d_{\text{HM}}) = \lambda_{S(L)} \frac{\gamma_{\text{SH(OH)}} \cdot a_{S(L)}}{d_{\text{HM}} + d_{\text{FM}}} \frac{\tanh(d_{\text{HM}}/2\lambda_{S(L)})}{n_1 + n_2 + Z_0 \cdot (\sigma_{\text{FM}} \cdot d_{\text{FM}} + \sigma_{\text{HM}} \cdot d_{\text{HM}})}, \quad (2)$$

where $a_{S(L)}$ is the injected current density, n_1 and n_2 are the substrate/air refractive indices, $Z_0 = 377 \ \Omega$ is vacuum impedance, and σ_{FM} and σ_{HM} are the terahertz

conductivities of the FM and HM layers, respectively. While the understanding on the propagation mechanisms of orbital currents is still lacking, our assumption of analogous behavior between spin and orbital currents provides a foundation for comparative analysis of key parameters (such as λ_L vs. λ_S). A more rigorous treatment of orbital transport would require theoretical development beyond the scope of this work.

For the AHE+MDE contribution, since the Ni layer thickness (d_{FM}) is fixed, the transverse terahertz current can be treated as a constant current source. Accounting for the optical absorption and shunting effects yields:

$$A_{\text{Ni}}(d_{\text{HM}}) = \frac{b \cdot d_{\text{Ni}}}{d_{\text{HM}} + d_{\text{Ni}}} \frac{1}{n_1 + n_2 + Z_0 \cdot (\sigma_{\text{Ni}} \cdot d_{\text{Ni}} + \sigma_{\text{HM}} \cdot d_{\text{HM}})}, \quad (3)$$

where b is an amplitude coefficient proportional to the net spin-current density and the AHE conversion efficiency in Ni³⁸. Detailed derivations are provided in Methods.

The temporal waveforms $\mathcal{E}_m(t)$ used in our model are constructed based on the experimental data. First, the waveform $\mathcal{E}_{\text{Ni}}(t)$ is directly extracted from the terahertz emission of the 5-nm Ni film and normalized to its peak amplitude (see SM Section S2). Second, for the waveforms corresponding to the spin and orbital signals - $\mathcal{E}_S(t)$ and $\mathcal{E}_L(t)$, we first analyze the terahertz spectra and phases from three representative samples: W(0.8)|Ni, W(6.6)|Ni and W(0.8)|Fe, as shown in Fig. 3a (thicknesses in parentheses are in nanometers). Notably, all three samples generate almost identical terahertz spectra, indicating that the emission spectra are largely independent of the underlying generation mechanism. However, a clear π phase shift between W(0.8)|Ni and the other two samples can be observed, leading to an opposite terahertz polarity for W(0.8)|Ni. The consistent phases between W(6.6)|Ni and W(0.8)|Fe further supports

our earlier conclusion that, when d_w is large (>3.0 nm), the terahertz emission from $W(d_w)|Ni$ is dominated by the ISHE-driven spin-to-charge conversion.

Given the nearly identical terahertz spectra across these samples, we adopt the experimentally measured waveform from the $HM|Fe$ heterostructure, denoted $\tilde{\mathcal{E}}_{S,\text{expt}}(t)$, as a common reference. The spin and orbital contributions $\mathcal{E}_S(t)$ and $\mathcal{E}_L(t)$ are then modeled by applying carrier-envelope phase (CEP) shifts φ_S and φ_L , to this reference waveform:

$$\mathcal{E}_{S(L)}(t) = \tilde{\mathcal{E}}_{S,\text{expt}} e^{i\varphi_{S(L)}} + c. c.. \quad (4)$$

In this model, the expected value of the spin-related CEP shift φ_S is zero. The CEP offset $\Delta\varphi = \varphi_L - \varphi_S$ thus represents the relative phase offset between the orbital and spin signals. In addition, we assume that both φ_S and φ_L are independent of the HM-layer thickness d_{HM} .

Substituting Eqs. (2-4) into Eq. (1) yields a fitting model to extract the key parameters of spin and orbital contributions. In this model, most variables ($n_1, n_2, \sigma_{FM}, \sigma_{HM}, \lambda_S, b$) can be determined either by consulting reference database or by direct measurements (see Methods and SM Section S4), leaving only 4 independent fitting parameters for each $HM|Ni$ sample: the orbital MPF in HM (λ_L), the ISHE/IOHE amplitude coefficients ($\tilde{A}_S = \gamma_{SH} \cdot a_S, \tilde{A}_L = \gamma_{OH} \cdot a_L$) and the CEP offset ($\Delta\varphi$).

Taking $W|Ni$ as an example, our model demonstrates excellent agreement with the experimental terahertz waveforms and amplitudes across a wide range of d_w , as shown in Figs. 3b1-b6. This agreement is further corroborated by the consistency between the modeled and measured terahertz intensities obtained via spectral integration (Fig. 3c).

Similar fitting agreements can be achieved for the Ta|Ni and Pt|Ni heterostructures (see SM Section S3). Figure 3d shows the absolute values of the extracted spin, orbital and Ni-layer contributions (A_S , A_L and A_{Ni}) in W|Ni as functions of d_W . These results quantitatively confirm our earlier mechanistic analysis: the orbital MFP ($\lambda_L=0.36$ nm) is substantially shorter than the spin MFP ($\lambda_S=2.20$ nm) in W.

Exclusion of Interfacial Rashba-Edelstein Effects

The observation of ultrashort orbital MFP raises the possibility that orbital-to-charge conversion may originate from interfacial mechanisms, such as the IOREE, which has been reported at W|SiO₂¹⁹ and Cu|MgO²¹ interfaces. Similarly, the inverse spin Rashba–Edelstein effect (ISREE) has been proposed as a potential source of terahertz emission^{43,44} (Fig. 4a). To evaluate whether such interfacial effects contribute significantly to the observed terahertz signals, we perform control experiments by inserting a 1-nm Cu spacer layer at either the W|Ni or SiO₂|W interface to intentionally disrupt possible interfacial conversion pathways.

In Fig. 4b, we compare the terahertz signals from three configurations: (i) the reference sample SiO₂|W(0.7)|Ni, (ii) SiO₂|W(0.7)|Cu(1)|Ni with Cu inserted at the W|Ni interface, and (iii) SiO₂|Cu(1)|W(0.7)|Ni with Cu inserted at the SiO₂|W interface. The W-layer thickness $d_W=0.7$ nm is chosen as it corresponds to the regime where orbital contributions dominate (peak positive amplitudes in Fig. 2a). Importantly, both the amplitude and waveform of the terahertz signals are barely affected by Cu insertion at either interface.

Although the results in Fig. 4b strongly suggest that interfacial conversion

mechanisms may play a negligible role, a more quantitative evaluation requires accounting for different emission components and their dependence on d_w . In Fig. 4c, we further plot the terahertz amplitudes as a function of d_w for all three configurations. All exhibit a consistent trend: a positive terahertz signal for $d_w < 3$ nm, peaking around $d_w = 0.7-0.8$ nm, followed by a monotonic decay in amplitude with increasing d_w . Interestingly, we observe that the Cu insertion affects the AHE contribution. Specifically, the $\text{SiO}_2|\text{Cu}(1)|\text{Ni}$ sample exhibits enhanced terahertz emission compared to $\text{SiO}_2|\text{Ni}$ (Fig. 4c). This enhancement could be attributed to increased spin currents in Ni, arising from either imbalanced spin-current reflections at the interfaces^{38,39}, or from the generation of a temperature gradient along z ^{45,46}.

After accounting for the AHE-signal variations, we find that the $\text{SiO}_2|\text{Cu}(1)|\text{W}(0.7)|\text{Ni}$ heterostructure retains $>60\%$ of the reference signal amplitude (Fig. 4c). The modest signal attenuation effectively *rules out* the IOREE or ISREE at the $\text{SiO}_2|\text{W}$ interface as dominant mechanisms. The residual reduction likely stems from charge-current shunting due to the Cu-layer insertion. Similarly, $\text{SiO}_2|\text{W}(0.7)|\text{Cu}(1)|\text{Ni}$ exhibits $\sim 60\%$ signal reduction (Fig. 4c), also ruling out dominant interfacial effects at the $\text{W}|\text{Ni}$ interface. Notably, considering the comparable shunting effects in the configurations (ii) and (iii), the difference in attenuation suggests that the 1-nm Cu spacer partially blocks the injected orbital currents.

In addition to amplitude variations, previous studies have reported substantial time delays (>80 fs) in terahertz signals with increasing d_w , which was attributed to ballistic-like transport time of orbital currents from the $\text{Ni}|\text{W}$ interface to the distant $\text{W}|\text{SiO}_2$

interface, ~ 20 nm away¹⁹. However, our sub-nanometer-resolution, thickness-dependent measurements on $\text{SiO}_2|\text{W}(d_{\text{W}})|\text{Ni}$ reveal negligible time shifts ($\sim 15 \pm 10$ fs) in the terahertz peak position, and no systematic increase in time delay is observed as d_{W} increasing from 3.2 to 15.2 nm (Fig. 4d). This conclusion is further supported by the generally shiftless terahertz waveforms across HM|Ni samples with the HM-layer thickness between 3 and 15 nm (Figs. 2b, e, and i). Together, these findings strongly exclude the IOREE at the $\text{SiO}_2|\text{W}$ interface – mediated by long-range orbital transport – as the dominant mechanism for terahertz emission.

Notably, we do observe substantial time shifts in the terahertz peak position up to ~ 250 fs, emerging only in the range of $d_{\text{W}}=2.0 - 3.5$ nm. As detailed in SM Section S5, we attribute this temporal anomaly to the destructive interference between the ISHE and IOHE signals in $\text{W}|\text{Ni}$, rather than ballistic transport effects. In contrast, no such temporal shift is observed for $\text{Ta}|\text{Ni}$ and $\text{Pt}|\text{Ni}$ heterostructures, where the destructive interference is absent. The exclusion of the IOREE and ISREE is crucial, because it indicates that the observed ultrashort orbital MFP is not limited by interfacial conversion processes, but rather represents the intrinsic transport length of L within W .

Discussion

Our fitting method enables quantitative separation of the ISHE and IOHE contributions in HM|Ni (see SM Section S3). In Fig. 5a, we summarize the amplitude coefficients \tilde{A}_{S} (spin) and \tilde{A}_{L} (orbital) extracted from $\text{W}|\text{Ni}$, $\text{Ta}|\text{Ni}$ and $\text{Pt}|\text{Ni}$. It is noteworthy that the polarities of \tilde{A}_{S} and \tilde{A}_{L} directly correlate with the intrinsic spin-Hall (γ_{SH}) and orbital-Hall (γ_{OH}) angles of each HM material. Importantly, the signs of

\tilde{A}_S and \tilde{A}_L in our experiments are consistent with the theoretical calculations for the spin-Hall and orbital-Hall conductivities (σ_{SH} and σ_{OH}), as shown in Fig. 5b, although the theoretical models exhibit marked variance in magnitude^{9,29,32}. This polarity consistency further validates our fitting model.

The fitting-derived parameters summarized in Table 1 provide deeper insight into the mechanisms underlying orbital-to-charge conversion in HMs. A key observation is that orbital currents exhibit consistently shorter MFPs than their spin counterparts ($\lambda_L < \lambda_S$) across all three HM materials (Ta, W and Pt). In particular, the orbital MFP in W is remarkably short ($\lambda_L \approx 0.35$ nm), corresponding to the scale of a single unit cell. For Ta and Pt, λ_L is 0.84 and 0.94 nm, respectively, spanning several unit cells. The fact that λ_L in Ta and Pt is comparable to λ_S suggests that a portion of the detected orbital-related signals from Ta|Ni and Pt|Ni may originate from spin currents, converted from the injected orbital currents via SOC near the Ni interfaces^{25,27}. Assuming that $\lambda_L \approx 0.35$ nm in W represents the intrinsic orbital MPF, we implement a convolution model, which suggests that $\sim 81\%$ and $\sim 48\%$ of the orbital currents could be converted to spin currents before their conversion to terahertz radiation via the ISHE in Ta and Pt, respectively (see SM Section S6).

Furthermore, despite its small value, the CEP offset, $\Delta\varphi$, is essential for accurately reproducing the experimental terahertz waveforms. This is particularly evident for the W|Ni sample with $d_W = 2-3$ nm, where the net terahertz signal is nearly canceled due to destructive interference between components. Without incorporating $\Delta\varphi$, the MC-TEM fails to reproduce the weak signal amplitude and waveform variation observed

experimentally. The physical origin of $\Delta\varphi$ remains an open question. One possible interpretation is that it corresponds to a time delay between the orbital-to-charge and spin-to-charge conversion processes in these HMs. For instance, in W, given that the terahertz center frequency is ~ 1.2 THz, the phase difference of ~ 0.016 rad corresponds to a time delay of ~ 2.1 fs. It is important to note that in our model, φ_S and φ_L are assumed to be dispersionless and independent of film thickness. A more precise determination of the conversion time difference would require broadband terahertz spectroscopy in combination with microscopic theoretical modeling to account for the underlying conversion dynamics.

In conclusion, our findings provide direct evidence for ultrashort orbital MFPs in HMs. By systematically analyzing terahertz emission from HM|Ni heterostructures, we rule out the interfacial IOREE as the dominant mechanism and confirm that orbital-to-charge conversion is primarily governed by the bulk IOHE. These results highlight the critical importance of understanding orbital-current propagation in ultrathin films, both for unraveling the mechanisms of orbital-to-charge conversion and for optimizing orbital-torque generation. While we demonstrate that orbital transport in HMs is highly localized, previous reports of long orbital MFPs in light metals such as Ti, Cr, and Cu^{11,21,30} suggest a potential material-dependent behavior that warrants further investigation.

Methods

Sample preparation and characterization. Wedge-shaped HM|FM heterostructures were fabricated on double-side-polished $\text{Al}_2\text{O}_3(0001)$ substrates. Prior to deposition, all substrates were annealed at 150°C for one hour in the sputtering chamber with a base pressure of 2×10^{-8} torr. A 4-nm SiO_2 buffer layer was first deposited onto the substrate. The HM|FM heterostructure was then deposit via DC magnetron sputtering at room temperature under an argon pressure of 3 mTorr. Finally, a 4-nm SiO_2 capping layers was deposited to prevent sample oxidation. The pre-deposition of a SiO_2 buffer layer ensures that the FM|HM heterostructure is encapsulated between SiO_2 layers. $\text{Al}_2\text{O}_3(0001)$ was selected as the substrate material for its high thermal conductivity, which helps mitigate the laser-induced heating and potential sample damage during measurements.

Prior to deposition, the deposition rates of W, Ta, and Pt were systematically calibrated using X-ray reflectometry. To precisely control the HM-layer thickness, wedge-shaped profiles were fabricated by controlling the deposition time during sputtering using a mechanical shutter. The shutter was moved in front of the sample surface at a constant, calibrated velocity, producing a continuous thickness gradient along x in the HM layer, over a lateral distance of 1.0 cm. In this study, the HM-layer thickness gradients were 1.60nm/mm for W, 2.50 nm/mm for Ta, and 1.33 nm/mm for Pt.

Post-deposition, the spatial variation in the HM-layer thickness along the x -axis was validated by measuring the transmission of a near-infrared femtosecond laser beam,

confirming the expected thickness gradient (see SM Section S1).

Experimental setup. Terahertz radiation was generated using a power-stabilized fiber oscillator (FIBRE SP, Nanjing Keyun Optoelectronics Ltd.), delivering laser pulses with a duration of 110 fs, a repetition rate of 36 MHz, a central wavelength of 1030 nm, and a maximum power of 3.3 W. In our experiments, a typical excitation power of ~ 0.7 W was used, with the beam incident from the substrate-side of the samples. An external magnetic field (H) of 1000 Oe was applied along the x -axis to saturate the magnetization of the FM layer.

The emitted terahertz waves were collected and focused by a pair of off-axis parabolic mirrors. The E_y component was selected by a terahertz polarizer, and was subsequently measured using the electro-optic sampling. A 1-mm-thick GaP was used as the detection crystal. To isolate the H -dependent signals and exclude potential signals from crystal anisotropy⁴⁷, we recorded the differential response by subtracting the signals measured under opposite magnetic-field directions ($+x$ and $-x$).

To investigate the HM-thickness-dependent terahertz emission, the sample was translated laterally along the x -axis with a step size of 0.1 mm, enabling spatial mapping across the HM wedge. The excitation beam was focused to a radius of 50 μm . Given the HM-layer thickness gradient of ~ 1.6 nm/mm, this configuration yields a thickness resolution of ~ 0.16 nm.

Multi-component terahertz emission model. In the frequency domain, the terahertz electric field $\tilde{\mathbf{E}}(\omega)$ is governed by the inhomogeneous wave equation⁴⁸:

$$-\nabla \times (\nabla \times \tilde{\mathbf{E}}) + \frac{n^2 \omega^2}{c^2} \tilde{\mathbf{E}} = -\frac{iZ_0 \omega}{c} \tilde{\mathbf{J}}, \quad (5)$$

where ‘ \sim ’ denotes the frequency-domain quantities, n is the refractive index, $\omega/2\pi$ is the terahertz frequency, c is the vacuum speed of light, and Z_0 is the vacuum impedance.

The total current density $\tilde{\mathbf{J}}$ comprises four primary contributions:

$$(1) \text{ ISHE, } \tilde{\mathbf{J}}_{\text{ISHE}} = \gamma_{\text{SH}} \tilde{\mathbf{J}}_S \times \mathbf{M}/|\mathbf{M}|,$$

$$(2) \text{ IOHE, } \tilde{\mathbf{J}}_{\text{IOHE}} = \gamma_{\text{OH}} \tilde{\mathbf{J}}_L \times \mathbf{M}/|\mathbf{M}|,$$

$$(3) \text{ AHE, } \tilde{\mathbf{J}}_{\text{AHE}} = \gamma_{\text{AHE}} \tilde{\mathbf{J}}_S \times \mathbf{M}/|\mathbf{M}|,$$

$$(4) \text{ MDE, } \tilde{\mathbf{J}}_{\text{MDE}} = (\partial_z \tilde{M}) \hat{y},$$

where $\tilde{\mathbf{J}}_S$ and $\tilde{\mathbf{J}}_L$ are the spin and orbital currents injected along the z -axis, \mathbf{M} is the FM magnetization (aligned along x), and \hat{y} is the unit vector in the x -direction. Under these conditions, all transverse current components ($\tilde{\mathbf{J}}_{\text{ISHE}}$, $\tilde{\mathbf{J}}_{\text{IOHE}}$, $\tilde{\mathbf{J}}_{\text{AHE}}$, and $\tilde{\mathbf{J}}_{\text{MDE}}$) are polarized along the y -axis.

The corresponding terahertz electric field $\tilde{E}(\omega)$, immediately behind the sample, can be calculated by the z -integration of the transverse charge current densities³⁷:

$$\tilde{E}(\omega) = eZ_{\text{eff}} \left\{ \int_0^{d_{\text{HM}}} [\gamma_{\text{SH}} \tilde{J}_S(\omega, z) + \gamma_{\text{OH}} \tilde{J}_L(\omega, z)] dz + \int_{-d_{\text{FM}}}^0 [\gamma_{\text{AHE}} \tilde{J}_S(\omega, z) + \partial_z \tilde{M}(\omega)] dz \right\}, \quad (6)$$

where Z_{eff} is the effective impedance, given by $Z_{\text{eff}} = \frac{Z_0}{n_1 + n_2 + Z_0 \cdot (\sigma_{\text{FM}} \cdot d_{\text{FM}} + \sigma_{\text{HM}} \cdot d_{\text{HM}})}$ ³⁷.

Here, we assume that the refractive indices of the substrate (n_1) and air (n_2), and the conductivities (σ_{FM} and σ_{HM}) are dispersionless within the relevant terahertz frequency range.

We then perform Fourier transform to obtain the time-domain terahertz field amplitudes $\tilde{E}(\omega) \rightarrow E(t)$, and evaluate the individual contributions from each mechanism. Since the FM-layer thickness d_{FM} is fixed and the HM-layer thickness d_{HM} is varied, the time-domain field amplitudes can be written as:

$$\begin{cases} E_S(t, d_{\text{HM}}) = eZ_{\text{eff}}(d_{\text{HM}}) \int_0^{d_{\text{HM}}} \gamma_{\text{SH}} j_S(t, z) dz \\ E_L(t, d_{\text{HM}}) = eZ_{\text{eff}}(d_{\text{HM}}) \int_0^{d_{\text{HM}}} \gamma_{\text{OH}} j_L(t, z) dz \\ E_{\text{Ni}}(t, d_{\text{HM}}) = eZ_{\text{eff}}(d_{\text{HM}}) \int_{-d_{\text{Ni}}}^0 [\gamma_{\text{AHE}} j_S(t, z) + \partial_z M(t, z)] dz \end{cases} . \quad (7)$$

The total time-domain electric field is then given by $E(t, d_{\text{HM}}) = E_S(t, d_{\text{HM}}) + E_L(t, d_{\text{HM}}) + E_{\text{Ni}}(t, d_{\text{HM}})$.

This model can be further simplified based on several key experimental observations. First, the ISHE waveform $E_S(t)$ is found to be almost invariant with respect to d_{HM} , as confirmed by measurements on the HM|Fe samples (see Figs. 2h-j), where only the amplitude changes while the temporal shape remains essentially unchanged. Second, since both AHE and MDE occur within the Ni layer, the waveform of $E_{\text{Ni}}(t)$ is also assumed to be independent of d_{HM} ; its amplitude variation primarily results from the shunting effect embedded in $Z_{\text{eff}}(d_{\text{HM}})$. Third, although the microscopic understanding of orbital transport remains less well understood, our experimental results – particularly those from Ta|Ni (Fig. 2e) – indicate that the spectral shape and phase of the IOHE signal are largely unaffected by variations in d_{HM} , justifying a similar assumption for $E_L(t)$.

Under these conditions, each terahertz-signal component can be factorized into a thickness-dependent amplitude $A_m(d_{\text{HM}})$ and a fixed temporal waveform $\mathcal{E}_m(t)$, such that: $E_m(t, d_{\text{HM}}) = A_m(d_{\text{HM}}) \cdot \mathcal{E}_m(t)$, with $m=S, L, \text{Ni}$. This decomposition leads directly to Eq. (1) in the main text.

In this formulation, the z -integration in Eq. (7) is applied to the spatial distributions of the underlying current sources $j_S(z), j_L(z)$, and $\partial_z M(z)$, while their temporal evolution determines the corresponding terahertz waveforms. Following Ref. 37, integration of

the spin currents $j_S(z)$ yields the amplitude term $A_S(d_{\text{HM}})$, presented in Eq. (2). By assuming an analogous behavior for the orbital current $j_L(z)$, we obtain the orbital contribution $A_L(d_{\text{HM}})$, also presented in Eq. (2). For the AHE and MDE components, the variation in d_{HM} affects only the effective impedance $Z_{\text{eff}}(d_{\text{HM}})$, leading to the amplitude term $A_{\text{Ni}}(d_{\text{HM}})$ as described in Eq. (3).

The waveform of $\mathcal{E}_{\text{Ni}}(t)$ is directly extracted from measurements on a 5-nm-thick Ni film (see SM Section S2). The waveforms for $\mathcal{E}_S(t)$ and $\mathcal{E}_L(t)$ are referred to the experimental waveform of the HM|Fe sample, with a relative CEP shift $\Delta\varphi$ introduced to account for the relative phase shifts between $\mathcal{E}_S(t)$ and $\mathcal{E}_L(t)$.

Parameter determination and fitting procedure. In the MC-TEM, several key parameters must be determined prior to fitting. First, the refractive index of air is fixed at $n_2=1$, while the refractive index of the substrate n_1 and the terahertz conductivities σ_{FM} and σ_{HM} are experimentally determined via terahertz transmission spectroscopy. Detailed experimental results are shown in SM Section S4. Second, the spin MFP λ_S in HM is independently extracted by fitting the terahertz amplitude from HM|Fe heterostructures as a function of the HM-layer thickness d_{HM} , using the ISHE amplitude expression $A_S(d_{\text{HM}})$ from Eq. (2)³⁷. The fitting results for W|Fe, Ta|Fe, and Pt|Fe are shown in Figs. 2a, 2d, and 2h, respectively. Finally, the amplitude coefficient b associated with the AHE+MDE contribution is determined from the terahertz signal of the HM|Ni wedge-shaped sample evaluated at $d_{\text{HM}}=0$, where the signal originates solely from the Ni layer. The above parameter values are provided in SM Table S2.

With these parameters are determined, we have 4 independent fitting variables

remain for each HM|Ni sample: the orbital MPF in HM (λ_L), the ISHE and IOHE amplitude coefficients ($\tilde{A}_S = \gamma_{SH} \cdot a_S$, $\tilde{A}_L = \gamma_{OH} \cdot a_L$) and the CEP offset ($\Delta\varphi$). These parameters are extracted by performing a global fitting procedure across all d_{HM} values using a genetic algorithm to minimize the deviation between the modeled and experimental terahertz waveforms. During this procedure, we impose an uncertainty of ± 0.05 rad on the spin-related CEP shift φ_S to account for possible deviations due to experimental uncertainties or subtle structural differences between the W|Ni and W|Fe samples. This uncertainty is propagated into the final error estimates shown in Table 1.

Acknowledgments: This work was accomplished in Fudan University. We acknowledge the support from the National Key Research and Development Program of China (Grant Nos. 2024FYA1408500, 2021YFA1400200, and 2022YFA1404700). We also acknowledge the support from the National Natural Science Foundation of China (Grant Nos. 12450407, 12274091, 12434003, and 12274083), and the support from the Shanghai Municipal Science and Technology (Grant No. 22JC1400200).

Table 1. Key parameters extracted using MC-TEM for different HMs.

	W	Ta	Pt
λ_S (nm)	2.20±0.13	1.34±0.07	2.00±0.34
λ_L (nm)	0.36±0.01	0.84±0.05	0.94±0.06
\tilde{A}_S ($\times 10^4$, arb. units)	-1.62±0.01	-0.57±0.46	0.68±0.24
\tilde{A}_L ($\times 10^4$, arb. units)	5.25±0.03	3.38±0.45	3.63±0.21
$\Delta\varphi$ (rad)	0.016±0.047	0.012±0.011	-0.045±0.016

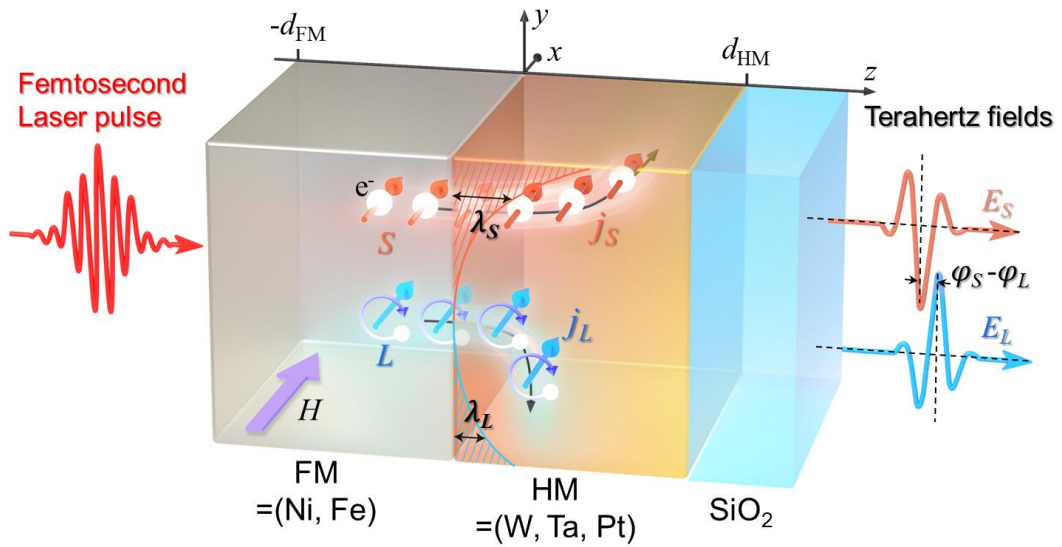


Figure 1. Schematic illustration of the experimental principle. Femtosecond laser excitations launches S and L propagation from the FM layer into the adjacent HM layer, leading to spin (j_S) and orbital (j_L) currents. These currents are converted into transverse charge currents via bulk conversion mechanisms: the ISHE for j_S and the IOHE for j_L , producing terahertz fields E_S and E_L , respectively. In the experiments, laser pulses are incident from the HM side of the sample. The geometry shown is illustrative. The directions of the resulting charge currents depend on the signs of the spin and orbital Hall angles (γ_{SH} and γ_{OH}) of the HM material. For illustrative purpose, the figure depicts the transverse charge currents from j_S and j_L as flowing in opposite directions. In reality, their relative directions vary: they are opposite in W and Ta, but aligned in Pt.

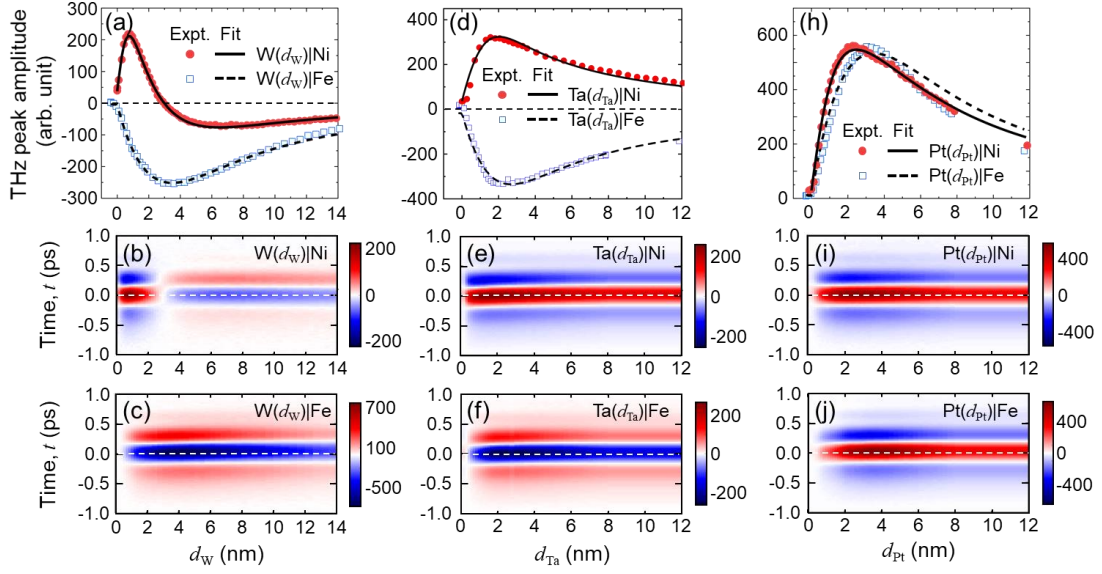


Figure 2. Terahertz emission as a function of HM-layer thickness in HM|FM heterostructures. **a.** Terahertz peak amplitudes extracted at $t=0$ as a function of the W-layer thickness d_W for W|Ni and W|Fe. Symbols represent experimental data, lines indicate fits based on MC-TEM. **b.** and **c.** Two-dimensional plots of terahertz waves at different d_W for W|Ni and W|Fe, respectively. **d – f.** Same as **a – c.**, but for Ta|Ni and Ta|Fe heterostructures. **h – j.** Same as **a – c.**, but for Pt|Ni and Pt|Fe heterostructures.

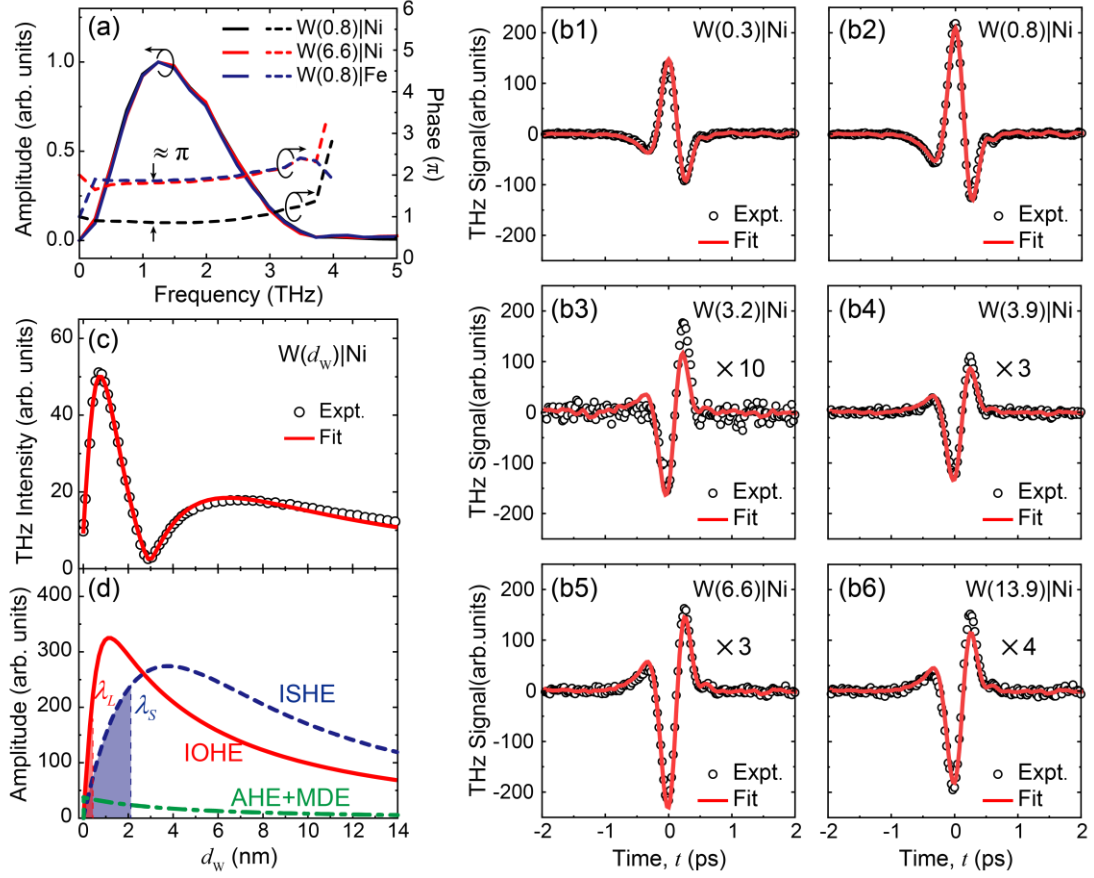


Figure 3. Fitting results using MC-TEM. **a.** Terahertz spectra and phases from W(0.8)|Ni, W(6.6)|Ni and W(0.8)|Fe samples. **b1- b6.** Fits to the time-domain terahertz waveforms from W|Ni samples with varying W-layer thickness (d_w) using MC-TEM. Symbols denote experimental data, and solid lines indicate model fits. **c.** Fitting of terahertz intensity (spectrally integrated) from W(d_w)|Ni as a function of d_w . Symbols represent experimental data, and lines indicate model fits. **d.** Extracted absolute amplitudes associated with the IOHE, ISHE and AHE+MDE contributions as a function of d_w . The orbital and spin MFPs are labeled.

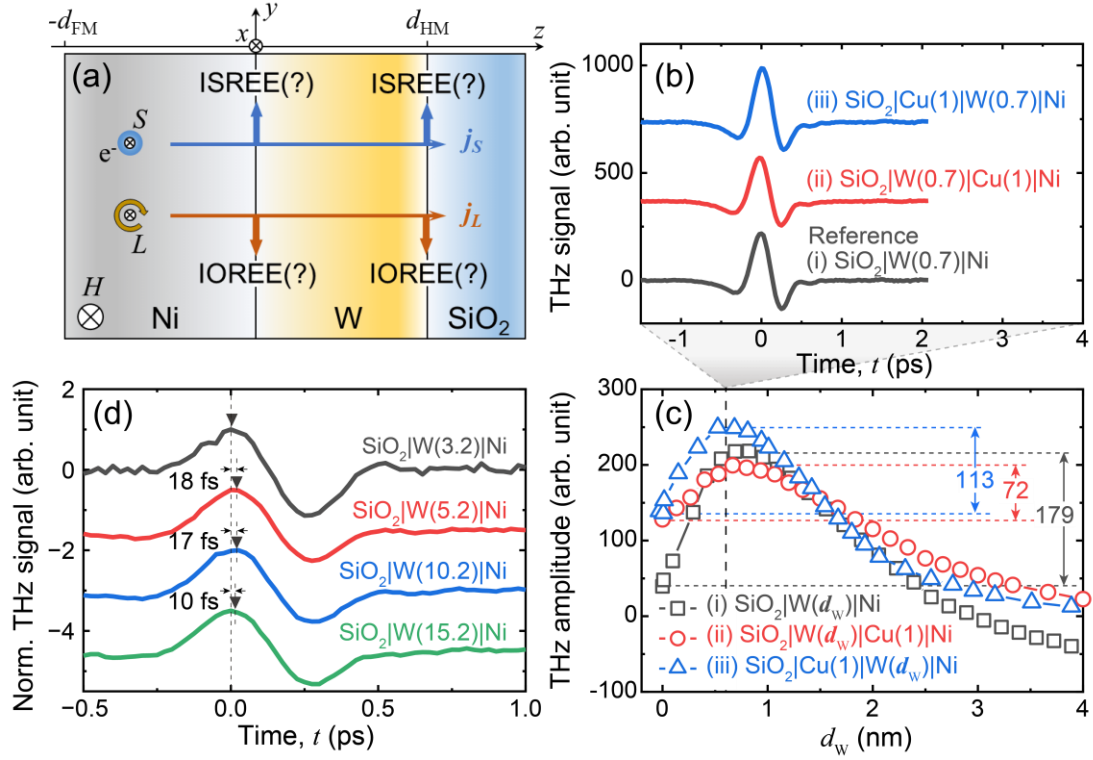


Figure 4. Exclusion of interfacial conversion mechanisms. **a.** Schematic illustration of potential interfacial conversion effects: the ISREE and IOREE at the W|Ni and SiO₂|W interfaces. **b.** Experimentally measured terahertz waveforms from three sample configurations: (i) SiO₂|W(0.7)|Ni, (ii) SiO₂|W(0.7)|Cu(1)|Ni (Cu inserted at W|Ni), and (iii) SiO₂|Cu(1)|W(0.7)|Ni (Cu inserted at SiO₂|W). **c.** Terahertz-field amplitudes extracted at $t=0$ as functions of W-layer thickness (d_w) from samples (i), (ii), and (iii). Amplitude differences between the signal maxima and values at $d_w=0$ are indicated. **d.** Normalized terahertz waveforms measured from SiO₂|W|Ni heterostructures with varying d_w . Peak positions and relative time shifts are denoted.

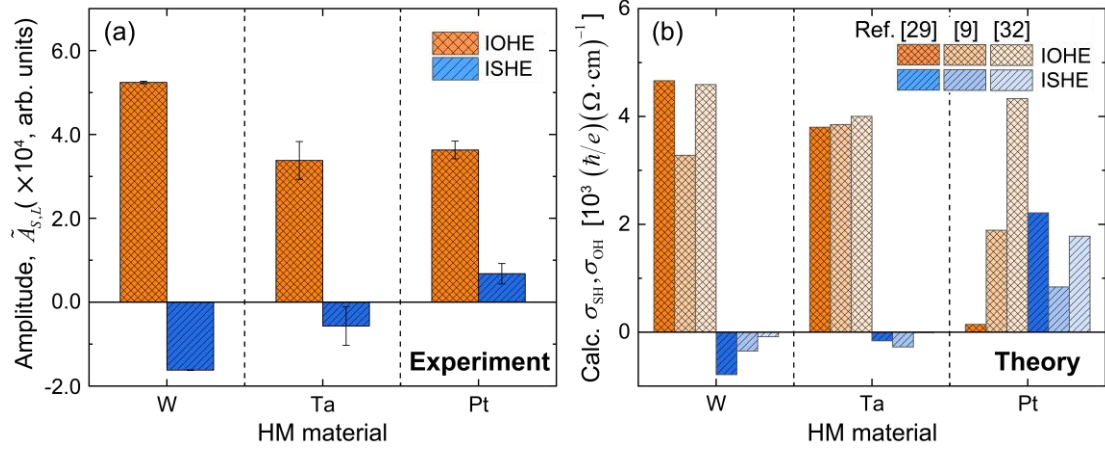


Figure 5. Distinguishing spin and orbital contributions. **a.** Extracted amplitude coefficients \tilde{A}_S (spin) and \tilde{A}_L (orbital) as a function of HM materials, obtained by fitting experimental data using the MC-TEM. **b.** *Ab-initio* calculated values of the spin Hall (σ_{SH}) and orbital Hall (σ_{OH}) conductivities for the corresponding HM materials^{9,29,32}.

References

1. Go, D. *et al.* Toward surface orbitronics: Giant orbital magnetism from the orbital Rashba effect at the surface of spmetals. *Sci. Rep.* **7**, 46742 (2017).
2. Phong, V. T. *et al.* Optically Controlled Orbitronics on a Triangular Lattice. *Phys. Rev. Lett.* **123**, 236403 (2019).
3. Bernevig, B. A., Hughes, T. L. & Zhang, S. C. Orbitronics: The intrinsic orbital current in p-doped silicon. *Phys. Rev. Lett.* **95**, 066601 (2005).
4. Go, D., Jo, D., Lee, H. W., Kläui, M. & Mokrousov, Y. Orbitronics: Orbital currents in solids. *EPL* **135**, 37001 (2021).
5. Zutic, I., Fabian, J. & Sarma, S. Das. Spintronics: Fundamentals and applications. *Rev. Mod. Phys.* **76**, 323–410 (2004).
6. Fert, A. Nobel lecture: Origin, development, and future of spintronics. *Rev. Mod. Phys.* **80**, 1517–1530 (2008).
7. Sinova, J., Valenzuela, S. O., Wunderlich, J., Back, C. H. & Jungwirth, T. Spin Hall effects. *Rev. Mod. Phys.* **87**, 1213–1260 (2015).
8. Go, D., Jo, D., Kim, C. & Lee, H. W. Intrinsic Spin and Orbital Hall Effects from Orbital Texture. *Phys. Rev. Lett.* **121**, 86602 (2018).
9. Kontani, H., Tanaka, T., Hirashima, D. S., Yamada, K. & Inoue, J. Giant orbital hall effect in transition metals: Origin of large spin and anomalous hall effects. *Phys. Rev. Lett.* **102**, 016601 (2009).
10. Salemi, L., Berritta, M., Nandy, A. K. & Oppeneer, P. M. Orbitaly dominated Rashba-Edelstein effect in noncentrosymmetric antiferromagnets. *Nat.*

- Commun.* **10**, 5381 (2019).
11. Choi, Y. G. *et al.* Observation of the orbital Hall effect in a light metal Ti. *Nature* **619**, 52–56 (2023).
 12. Ding, S. *et al.* Observation of the Orbital Rashba-Edelstein Magnetoresistance. *Phys. Rev. Lett.* **128**, 67201 (2022).
 13. Ding, S. *et al.* Harnessing Orbital-to-Spin Conversion of Interfacial Orbital Currents for Efficient Spin-Orbit Torques. *Phys. Rev. Lett.* **125**, 177201 (2020).
 14. Liao, L. *et al.* Efficient orbital torque in polycrystalline ferromagnetic-metal/Ru/Al₂O₃ stacks: Theory and experiment. *Phys. Rev. B* **105**, 104434 (2022).
 15. Lyalin, I., Alikhah, S., Berritta, M., Oppeneer, P. M. & Kawakami, R. K. Magneto-Optical Detection of the Orbital Hall Effect in Chromium. *Phys. Rev. Lett.* **131**, 156702 (2023).
 16. Bose, A. *et al.* Detection of long-range orbital-Hall torques. *Phys. Rev. B* **107**, 134423 (2023).
 17. Hayashi, H. *et al.* Observation of long-range orbital transport and giant orbital torque. *Commun. Phys.* **6**, 32 (2023).
 18. Go, D. *et al.* Long-Range Orbital Torque by Momentum-Space Hotspots. *Phys. Rev. Lett.* **130**, 246701 (2023).
 19. Seifert, T. S. *et al.* Time-domain observation of ballistic orbital-angular-momentum currents with giant relaxation length in tungsten. *Nat. Nanotechnol.* **18**, 1132–1138 (2023).

20. Mishra, S. S., Lourembam, J., Lin, D. J. X. & Singh, R. Active ballistic orbital transport in Ni/Pt heterostructure. *Nat. Commun.* **15**, 4568 (2024).
21. Xu, Y. *et al.* Orbitronics: light-induced orbital currents in Ni studied by terahertz emission experiments. *Nat. Commun.* **15**, 2043 (2024).
22. Zheng, Z. C. *et al.* Magnetization switching driven by current-induced torque from weakly spin-orbit coupled Zr. *Phys. Rev. Res.* **2**, 013127 (2020).
23. Boeglin, C. *et al.* Distinguishing the ultrafast dynamics of spin and orbital moments in solids. *Nature* **465**, 458–461 (2010).
24. Idrobo, J. C. *et al.* Direct observation of nanometer-scale orbital angular momentum accumulation. arxiv.org/abs/2403.09269 (2025).
25. Urazhdin, S. Symmetry constraints on orbital transport in solids. *Phys. Rev. B* **108**, L180404 (2023).
26. Belashchenko, K. D. *et al.* Breakdown of the drift-diffusion model for transverse spin transport in a disordered Pt film. *Phys. Rev. B* **108**, 144433 (2023).
27. Rang, M. & Kelly, P. J. Orbital relaxation length from first-principles scattering calculations. *Phys. Rev. B* **109**, 214427 (2024).
28. Salemi, L., Berritta, M. & Oppeneer, P. M. Quantitative comparison of electrically induced spin and orbital polarizations in heavy-metal/ 3d -metal bilayers. *Phys. Rev. Mater.* **5**, 74407 (2021).
29. Go, D., Lee, H. W., Oppeneer, P. M., Blügel, S. & Mokrousov, Y. First-principles calculation of orbital Hall effect by Wannier interpolation: Role of

- orbital dependence of the anomalous position. *Phys. Rev. B* **109**, 174435 (2024).
30. Lee, S. *et al.* Efficient conversion of orbital Hall current to spin current for spin-orbit torque switching. *Commun. Phys.* **4**, 234 (2021).
 31. Lee, D. *et al.* Orbital torque in magnetic bilayers. *Nat. Commun.* **12**, 6710 (2021).
 32. Salemi, L. & Oppeneer, P. M. First-principles theory of intrinsic spin and orbital Hall and Nernst effects in metallic monoatomic crystals. *Phys. Rev. Mater.* **6**, 095001 (2022).
 33. Leitenstorfer, A., Hunsche, S., Shah, J., Nuss, M. C. & Knox, W. H. Detectors and sources for ultrabroadband electro-optic sampling: Experiment and theory. *Appl. Phys. Lett.* **74**, 1516–1518 (1999).
 34. Wu, Q. & Zhang, X. C. Free-space electro-optic sampling of terahertz beams. *Appl. Phys. Lett.* **67**, 3523 (1995).
 35. Kampfrath, T. *et al.* Terahertz spin current pulses controlled by magnetic heterostructures. *Nat. Nanotechnol.* **8**, 256–260 (2013).
 36. Yang, D. *et al.* Powerful and Tunable THz Emitters Based on the Fe/Pt Magnetic Heterostructure. *Adv. Opt. Mater.* **4**, 1944–1949 (2016).
 37. Seifert, T. *et al.* Efficient metallic spintronic emitters of ultrabroadband terahertz radiation. *Nat. Photonics* **10**, 483–488 (2016).
 38. Zhang, Q. *et al.* Terahertz Emission from Anomalous Hall Effect in a Single-Layer Ferromagnet. *Phys. Rev. Appl.* **12**, 054027 (2019).

39. Mottamchetty, V. *et al.* Direct evidence of terahertz emission arising from anomalous Hall effect. *Sci. Rep.* **13**, 5988 (2023).
40. Liu, Y. *et al.* Separation of emission mechanisms in spintronic terahertz emitters. *Phys. Rev. B* **104**, 064419 (2021).
41. Beaurepaire, E. *et al.* Coherent terahertz emission from ferromagnetic films excited by femtosecond laser pulses. *Appl. Phys. Lett.* **84**, 3465–3467 (2004).
42. Zhang, W. *et al.* Ultrafast terahertz magnetometry. *Nat. Commun.* **11**, 4247 (2020).
43. Jungfleisch, M. B. *et al.* Control of Terahertz Emission by Ultrafast Spin-Charge Current Conversion at Rashba Interfaces. *Phys. Rev. Lett.* **120**, 207207 (2018).
44. Zhou, C. *et al.* Broadband Terahertz Generation via the Interface Inverse Rashba-Edelstein Effect. *Phys. Rev. Lett.* **121**, 086801 (2018).
45. Feng, Z. *et al.* Anomalous Nernst Effect Induced Terahertz Emission in a Single Ferromagnetic Film. *Nano Lett.* **23**, 8171–8179 (2023).
46. Zhang, H. *et al.* Tuning terahertz emission generated by anomalous Nernst effect in ferromagnetic metal. *Appl. Phys. Rev.* **10**, 021417 (2023).
47. Zhang, S. *et al.* Nonrelativistic and nonmagnetic terahertz-wave generation via ultrafast current control in anisotropic conductive heterostructures. *Adv. Photonics* **5**, 056006 (2023).
48. Jackson, J. D. *Classical Electrodynamics*. (American Association of Physics Teachers, 1999).